APS physics

CHORUS

This is the accepted manuscript made available via CHORUS. The article has been published as:

Theory of microphase separation in bidisperse chiral membranes

Raunak Sakhardande, Stefan Stanojeviea, Arvind Baskaran, Aparna Baskaran, Michael F. Hagan, and Bulbul Chakraborty

Phys. Rev. E **96**, 012704 — Published 13 July 2017

DOI: 10.1103/PhysRevE.96.012704

Theory of microphase separation in bidisperse chiral membranes

Raunak Sakhardande, Stefan Stanojeviea, Arvind Baskaran,
Aparna Baskaran, Michael F. Hagan,* and Bulbul Chakraborty
Martin Fisher School of Physics, Brandeis University, Waltham, MA 02453, USA
(Dated: June 20, 2017)

We present a Ginzburg-Landau theory of microphase separation in a bidisperse chiral membrane consisting of rods of opposite handendness. This model system undergoes a phase transition from an equilibrium state where the two components are completely phase separated to a state composed of microdomains of a finite size comparable to the twist penetration depth. Characterizing the phenomenology using linear stability analysis and numerical studies, we trace the origin of the discontinuous change in microdomain size that occurs during this phase transition to a competition between the cost of creating an interface and the gain in twist energy for small microdomains in which the twist penetrates deep into the center of the domain.

I. INTRODUCTION

When two immiscible fluids are mixed, they typically undergo bulk phase separation. Applications ranging from food science, catalysis, and the function of cell membranes require the arrest of this phase separation to form microstructures. A common pathway to accomplish this is to introduce a third component, such as a surfactant, that stabilizes interfaces between the two fluids [1]. Here, we theoretically demonstrate a novel mechanism for microphase separation in fluid membranes that is mediated by the chirality of the constituent entities themselves, and hence does not require the introduction of a third component. In addition to identifying a design principle to engineer nano structured materials, this work could shed light on the role of chirality in compositional fluctuations and raft formation in biomembranes [2–7].

Our theory is motivated by a recently developed colloidal-scale model system of fluid membranes, composed of fd-virus particles [8–13]. The system contains two species of virus particles that have opposite chirality and different lengths (Fig 1). In the presence of a depletant, they self-assemble into a monolayer membrane that is one rod length thick. The competition between depletant entropy, mixing entropy of the two species, and molecular packing forces leads to a rich phase behavior within a membrane, including bulk phase separation of the two species, microdomain formation, and homogeneous mixing. In particular, the experiments find that in the regime where a single species forms a macroscopic membrane, limited only by the amount of material, a mixture of two species leads to the formation of circular monodisperse microdomains (rafts) of one species in a background of the other. Recently, Xie et al. [14] showed that, given the existence of such microdomains, chirality mediates repulsive interactions between domains. Here, we consider the forces that allow such microdomains to exist at equilibrium by stabilizing them at a finite size.

To understand the mechanisms controlling microdomain formation, we develop a continuum Ginzburg-Landau theory that captures the physics of chirality and compositional fluctuation in a 2D binary mixture of rods with opposing chiralities. The primary physics that we incorporate into the theory is a coupling between the twist of the director field and the compositional fluctuations [15]. By using linear stability analysis and numerical solutions of the time-dependent Ginzburg-Landau equations, we show that the tendency of the molecules to twist arrests the phase separation of the two species, and stabilizes a microdomain phase whose phenomenology closely mimics that observed in experiments. In particular, the theory shows a discontinuous jump in the microdomain radius as the system transitions from a microphase separated state to bulk separation, a phenomenon observed in the experiments as well. In contrast, previously studied mechanisms of microphase separation lead to a domain size that continuously diverges as the system approaches bulk phase separation [16–19]. Moreover, while previous work showed that the incompatibility between chiral packing and crystalline order leads to self-limited filamentous bundles [20, 21], our work demonstrates the emergence of chiral-mediated microdomains in liquid-liquid phase separation.

II. MODEL

The Ginzburg-Landau (GL) model involves two fields: a director field $\hat{\mathbf{n}}(\mathbf{r})$ that characterizes the orientation of the rods with respect to the membrane normal and a pseudo-scalar field $\psi(\mathbf{r})$, which characterizes the difference in densities of the two species of rods with opposing chiralities [15]. We choose a coordinate system in which the layer normal of the membrane lies along the z axis and normalize the order parameter ψ such that $\psi = \pm 1$ correspond to the homogeneous one-component phases.

* hagan@brandeis.edu

The GL functional is taken to be of the form:

$$\beta F = \int d^2\mathbf{r}\left[\frac{1}{2}K_1(\nabla\cdot\hat{\mathbf{n}})^2 + \frac{1}{2}K_2\left(\hat{\mathbf{n}}\cdot\nabla\times\hat{\mathbf{n}} - q\left(\psi\right)\right)^2 + \frac{1}{2}K_3\left(\hat{\mathbf{n}}\times\nabla\times\hat{\mathbf{n}}\right)^2 + \frac{C}{2}\sin^2\theta - \frac{\psi^2}{2} + \frac{\psi^4}{4} + \frac{\lambda_\psi}{2}\left(\nabla\psi\right)^2\right]$$

The physics incorporated in the GL functional can be summarized as follows: i) The first three terms arise from the Frank elasticity associated with director distortion, with K_1, K_2 and K_3 being the elastic constants associated with splay, twist and bend respectively [22]. The twist term involves a pitch $q(\psi(\mathbf{r}))$ that encodes the chirality and hence the associated tendency of the rods to develop a spontaneous non-zero twist. In a mixture of left and right handed rods, q is naturally a function of the composition, which introduces a coupling between $\hat{\mathbf{n}}(\mathbf{r})$ and $\psi(\mathbf{r})$. ii) The term $\frac{C}{2}\sin^2\theta$ encodes the fact that the rods in the membrane tend to align with the layer normal [22], and gives rise to the standard mechanism of twist expulsion seen in Smectic C systems. When $\psi = \pm 1$, the terms discussed in (i) and (ii) reduce to the theoretical description used successfully to describe single component chiral membranes in earlier works [23–25]. iii) The compositional fluctuations encoded in the field ψ are described by a standard ψ^4 theory *below* the critical point that leads to bulk phase separation, with an energetic cost to forming interfaces controlled by the parameter λ_ψ. Thus, the difference in the length of the rods that leads to phase separation in the experimental system is represented as an effective interaction, and our 2D model does not include information about the spatial variation of the membrane in the third dimension. Such height fluctuations were recently theoretically considered in the context of single-species membranes [26]. Moreover, our results neglecting height fluctuations are qualitatively consistent with those of Ref. [27], which appeared after the initial version of this manuscript was made public and does include height fluctuations in a description colloidal raft formation. Consistent with that comparison, we find that including height fluctuations in our theory does not qualitatively change the results.

In the following, we work in the single elastic constant approximation of the Frank elasticity: $K_1 = K_2 = K_3 \equiv K$. We model the variation of q with composition through a minimal linear coupling, $q(\psi) = q_0 + a\psi$, which is allowed by symmetry and defines the coupling parameter a. We nondimensionalize the GL functional using the twist penetration depth $\lambda_t \equiv \sqrt{\frac{K}{C}}$ as the characteristic length scale. To minimize the number of parameters, we choose the same values for K and C for each species. A different choice would lead to a different twist penetration length inside and outside of domains [14] but would not qualitatively change our results. We then define $\psi' = \frac{\psi}{(1-Ka^2)^{1/2}}$ to absorb the (uninteresting) ψ^2 term which arises from the coupling between twist and composition, rescale βF by $(1-Ka^2)^{-2}$, and define the dimensionless parameters:

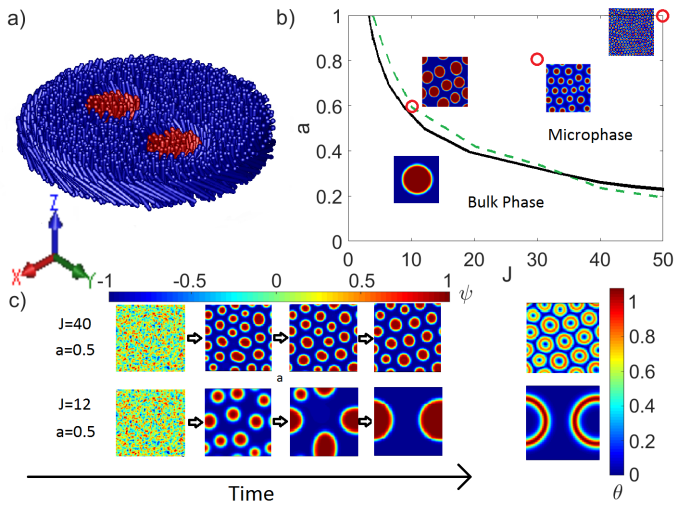

FIG. 1. (color online) a) Schematic of the experimental system. b) The primary results of this work summarized in a phase diagram as a function of the smectic alignment parameter J and the twist-composition coupling parameter a. The lines indicate the phase boundary between the microphase separated and bulk phase separated states as obtained from linear stability analysis (black/solid) and numerical integration of Eqs. 2-3 (green/dashed). The snapshots show configurations at steady state obtained from numerics at the indicated parameter values (o). c) Illustration of the evolution to steady state for two parameter sets. The left panel shows the evolution of the composition field, and the right panel shows the twist profiile in the steady state. The results shown here and in the rest of the main text are for a 60-40 mixture with $\lambda_\psi = 0.1$, and $q_0 = 0.1$

$a' = a\left(1-Ka^2\right)^{1/2}$, $\lambda'_\psi = \frac{\lambda_\psi/\lambda_t^2}{(1-Ka^2)}$, $J = \frac{K}{(1-Ka^2)^2}$, and $q'_0 = q_0(1-Ka^2)$.

The GL functional then becomes:

$$\begin{aligned}
\beta F &= \int d^2\mathbf{r}'\left[f_{\rm LC} + f_\psi + f_{\rm Cross}\right] \\
f_{\rm LC} &= \frac{J}{2}\left[\left(\nabla'\cdot\hat{\mathbf{n}}\right)^2 + \left(q_0'^2 - 2q'_0\hat{\mathbf{n}}\cdot\nabla'\times\hat{\mathbf{n}}\right) + \left(\nabla'\times\hat{\mathbf{n}}\right)^2 + sin^2(\theta)\right] \\
f_\psi &= \left[-\frac{\psi'^2}{2} + \frac{\psi'^4}{4} + \frac{\lambda'_\psi}{2}\left(\nabla'\psi'\right)^2\right] \\
f_{\rm Cross} &= \left[-Ja'\psi'\left(\hat{\mathbf{n}}\cdot\nabla'\times\hat{\mathbf{n}}\right) + Ja'q'_0\psi'\right] \qquad (1)
\end{aligned}$$

This nondimensionalized GL functional is used in all of our subsequent analysis, and the $'$'s are dropped for compactness of notation.

We model the dynamics by the time-dependent GL equations with a conserved composition field ψ: $\partial_t\psi = \nabla^2\frac{\delta F}{\delta\psi}$ (Model B dynamics), and a non-conserved director field $\partial_t\hat{\mathbf{n}} = -\left(\mathbf{I} - \hat{\mathbf{n}}\hat{\mathbf{n}}\right)\cdot\frac{\delta F}{\delta\hat{\mathbf{n}}}$ (Model A dynamics)[28]. The $\hat{\mathbf{n}}$ dynamics accounts explicitly for the fact that it is a unit vector. The time constants for the relaxation dynamics of ψ and $\hat{\mathbf{n}}$ have been chosen to be same and

set equal to 1. The resulting equations are :

$$\partial_t \psi = \nabla^2 \left(-\psi + \psi^3 - \lambda_\psi \nabla^2 \psi - Ja\left(\hat{\mathbf{n}} \cdot \nabla \times \hat{\mathbf{n}}\right) + Jaq_0\right) \quad (2)$$

$$\partial_t \hat{\mathbf{n}} = -\left(\mathbf{I} - \hat{\mathbf{n}}\hat{\mathbf{n}}\right) \cdot \left(-J\nabla^2 \hat{\mathbf{n}} - 2Jq\nabla \times \hat{\mathbf{n}} + J\hat{\mathbf{n}} \times \nabla q + J(n_x \hat{x} + n_y \hat{y})\right) \quad (3)$$

III. LINEAR STABILITY ANALYSIS

Eqs.(2-3) admit homogenous steady states of the form $\psi = \pm 1$ and $\hat{\mathbf{n}} = \hat{\mathbf{z}}$. As a first step in understanding the dynamics of phase separation, we analyze the instability of the homogeneous state to small fluctuations of the form $\psi = 1 + \delta\psi$ and $\hat{\mathbf{n}} = \hat{\mathbf{z}} + \delta\mathbf{n}$. [29] We introduce Fourier transformed variables $\widetilde{X}(\mathbf{k}, t) = \int d^2\mathbf{r} e^{i\mathbf{k}\cdot\mathbf{r}} X(\mathbf{r}, t)$. Without loss of generality, we choose a coordinate system in the plane of the membrane such that the x axis lies along the spatial gradient direction. We find that the longitudinal fluctuations in the director $\delta\widetilde{n}_x$ decouple from the other variables (Appendix B) and we obtain the linearized equations

$$\partial_t \begin{pmatrix} \delta\widetilde{\psi} \\ \delta\widetilde{n}_y \end{pmatrix} = \begin{pmatrix} -2k^2 - \lambda_\psi k^4 & ik^3 Ja \\ -ikJa & -J - Jk^2 \end{pmatrix} \begin{pmatrix} \delta\widetilde{\psi} \\ \delta\widetilde{n}_y \end{pmatrix} \quad (4)$$

The homogeneous state is found to be linearly unstable to modes k that satisfy

$$\lambda_\psi k^6 - (Ja^2 - 2 - \lambda_\psi)k^4 + 2k^2 < 0 \; . \quad (5)$$

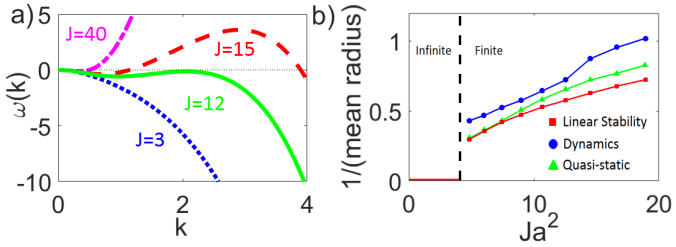

FIG. 2. (color online) a) The largest eigenvalue $\omega(k)$ of the linear stability matrix in Eq.(4) as a function of the wavevector k for indicated values of the alignment strength J, with $a = 0.5$ and $\lambda_\psi = 0.1$. b) Dependence of the optimal microdomain size on Ja^2 obtained by three different analysis methods: the steady-state mean radius of microdomains obtained by numerical integration(upper line), the radius which minimizes the GL free energy (calculated as described in the text) (middle line), and wavelength corresponding to the fastest-growing mode calculated by linear stability analysis (lower line), for $\lambda_\psi = 0.1$. Throughout this manuscript, all lengths are given in units of the twist penetration length λ_t.

We see from Eq. 5 that the $k = 0$ mode is always marginally stable, and that the linear instability is controlled only by the combination Ja^2 and does not depend individually on the strengths of the smectic alignment and the twist-composition coupling. At a critical value of Ja^2 determined by $(Ja^2 - 2 - \lambda_\psi)^2 = 8\lambda_\psi$, the mode with $k_f = (2/\lambda_\psi)^{1/4}$ becomes unstable (see Appendix B). For parameters at or beyond the critical value, the average microdomain radius can be estimated as $r = 2\pi/k_f$, where k_f is the fastest growing mode. Fig. 2 shows the largest eigenvalue $\omega(k)$ of the linear stability matrix in Eq.(4) for different parameters. For any non-zero value of λ_ψ, the instability occurs at a finite k, which demonstrates that the instability of the homogeneous phase is to microdomains of a finite size. The transition from a macroscopically phase separated state (infinite domain size, $k = 0$) to a microphase separated state should thus be accompanied by a discontinuity in the domain size (see Appendix B).

Numerical analysis of Eqs.(2-3) verifies this discontinuous change in the domain size. We solve Eqs.(2-3) numerically by using an implicit convex splitting scheme to evolve the equation for ψ and the forward Euler method to evolve the director field (see Appendix E). We initialize the system with random compositional fluctuations around a homogeneous mixture with $\psi = 0.2$ and we explore the phase space spanned by J and a. For most of the results shown here, we choose $\lambda_\psi = 0.1$, as the interface width in the experiments is found to be much smaller than the twist penetration length [12]. As shown in section IV and Fig. 6 of Appendix C, changing λ_ψ leads to quantitative but not qualitative changes. Also, we set $q_0 = 0.1$ as the preferred chiral twists of the two species of rods in the experimental system are not equal. The phase diagram obtained from numerics is shown in Fig. 1. It is evident that linear stability analysis captures all qualitative aspects of the numerically determined phase diagram. The steady state domain sizes obtained from numerics are shown in Fig. 2 and clearly demonstrate the discontinuous change accompanying the phase transition. We note however that the effect of q_0 on the phase transition is not captured by the linear stability analysis since this parameter enters only at higher order (see Fig. 8, Appendix D).

The formation of finite-sized microdomains is controlled by a competition between chirality and interfacial tension. A similar competition exists even in a chiral membrane of a single species, where the interfacial tension exists between the membrane edge and the bulk polymer suspension. A theoretical analysis of this system [23] showed a transition between membranes of finite size and unbounded macroscopic membranes. Within such a membrane, the twist is expelled to the edge, decaying over a length λ_t, and the membrane size grows continuously as the transition is approached. Here we see that introducing a second species with opposite handedness into such a membrane provides a mechanism for the twist to penetrate the interior of the membrane. As shown in Fig. 1, the director twists at the edge of each domain, and then untwists (twists in the opposite direction) into the background. This twist is confined to within approx-

imately λ_t of a domain edge. The ability of the interface to accommodate twist is the mechanism that leads to the formation of microdomains in the region of parameter space where each species by itself would form a macroscopic membrane.

To quantitatively unfold this mechanism, and to understand the discontinuous change in domain size that occurs at the transition, we examine how the spatial variations in ψ and $\hat{\mathbf{n}}$ influence the free energy Eq. (1). To this end, we calculate the free energy of a domain of radius R of one species in a background of the other. We do so by assuming profiles for ψ and $\hat{\mathbf{n}}$ that are consistent with the results obtained from numerical integration (see Appendix B). The optimal domain size is then determined by the value of R at each J, a, q_0, λ_ψ, for which the free energy is minimized (Fig. 3). The resulting domain sizes are consistent with those obtained from linear stability analysis and numerical integration (Fig. 2). Note that, by considering a single droplet embedded in an infinite membrane, we are neglecting inter-domain interactions in this calculation. This assumption is consistent with the fact that inter-domain interactions have a range of λ_t (distance over which twist penetrates in the background) and therefore are small for larger spacings between domains. This assumption is also consistent with the experimental observation of Sharma et al. that the preferred domain size is independent of inter-droplet spacing (Fig. 4 a-c of Ref. [12]).

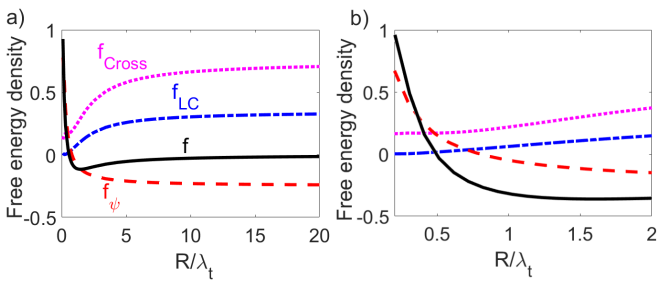

FIG. 3. (color online) a) The free energy density in a domain f (solid/black), along with the separate contributions ($f_{\rm LC}$ (dot-dashed/blue), f_ψ (dashed/red) and $f_{\rm Cross}$ (dotted/pink)) are shown as a function of domain radius R, measured in units of λ_t, for $J = 30$ and $a = 0.7$. The domain radius is varied from $0.2\lambda_t$ to $20\lambda_t$. b) The same free energy density contributions as in (a) but focusing on the behavior at small R.

The origin of the discontinuity in domain size is revealed by examining the variations in different contributions to the free energy density ($f_{\rm LC}$, f_ψ and $f_{\rm Cross}$) as the microdomain size changes. Fig. 3 shows these variations for a parameter set in the microphase separation regime. Note that in an extensive system with clear scale separation between bulk and interface, the interfacial contribution to a free energy density decays with increasing domain size, while the bulk contribution remains constant. In contrast, we see that $f_{\rm LC}$ and $f_{\rm Cross}$ are superextensive for small domain sizes, only becoming extensive asymptotically. This superextensivity is significant only for domain sizes of the order of the twist penetration length ($R \sim 5\lambda_t$). Thus, finite-sized microdomains appear only when the increase in $f_{\rm LC}$ and $f_{\rm Cross}$ with R is sufficient to outcompete f_ψ at these small domain sizes. As Ja^2 decreases, the super-extensive behavior diminishes, forcing the critical domain size (at which $f_{\rm LC}$ and $f_{\rm Cross}$ dominate over f_ψ) to larger R. At the threshold value of Ja^2, $f_{\rm LC}$ and $f_{\rm Cross}$ become extensive before dominating over the interfacial tension, and macrophase separation sets in.

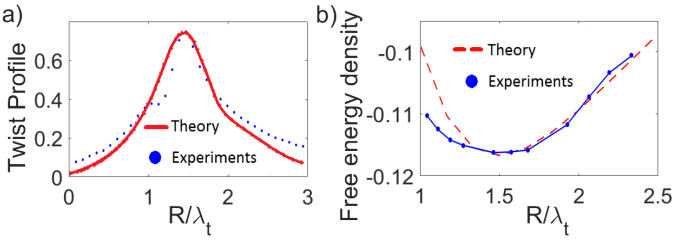

FIG. 4. (color online) a) The theoretical twist profile obtained from dynamical analysis is compared with the one obtained from the experiments [12]. b) The theoretical free energy density profile as a function of the microdomain radius for the parameters $J = 20$ and $a = 0.7$ is compared against the experimentally determined free energy. The radius is in units of the twist penetration length observed in the experiments: $\lambda_t = 0.48\mu m$. The theoretical free energy has also been shifted to match the experimental curve at the minimum.

The source of the super-extensive growth in $f_{\rm LC}$ and $f_{\rm Cross}$ can be understood from the dependence of twist profiles on R. For large R, twist decays exponentially from the domain edge (Fig. 6 in Appendix C); thus ensuring scale separation between the bulk and the interface. On the other hand, such a separation does not exist for small microdomains where the twist penetrates to the center of the domain.

IV. COMPARISON WITH EXPERIMENTS

Finally, we assess the ability of our theory to reproduce experimental measurements on the *fd*-virus system. We first estimate values of J and a corresponding to the experimental system by fitting against the experimentally measured twist profile (Fig. 4a); specifically, a is determined by the maximum twist at the edge of a microdomain and J is then determined by its radius. In Fig. 4b we then compare the free energy as a function of microdomain size estimated by the quasi-static calculation described above against the experimental free energy, which was determined from the dependence of growth and shrinkage rates on domain size. We see that

the calculation closely matches the experiments for larger than average domains but underestimates the probability of observing smaller microdomains. We do not understand the source of this discrepancy. However, one possibility is the neglect of the length difference between the two species in our theoretical analysis.

In conclusion, we have presented a theory of microphase separation in membranes, which is driven by chirality of its constituent entities. The underlying mechanism of microphase separation can be traced to the gain in twist energy in these structures, which can accommodate twist at the interfaces. We have provided quantitative analysis that unfolds the precise factors leading to the appearance of microdomains. We have also shown that the microdomains have a natural length scale determined by the twist penetration depth, and therefore the domain size does not increase continuously as the system transitions to the macrophase separated state. Microdomains that are much larger than the twist penetration depth fail to gain enough free energy from the twisting at the interface to compensate for the free energy cost of creating an interface where the composition changes. By reducing λ_ψ, this limiting length can be made larger, however the transition is discontinuous for all finite values of λ_ψ. This feature of the microdomains is appealing from the perspective of creating nanostructures since the domain size can be tightly controlled.

V. ACKNOWLEDGMENT:

This work was supported by the Brandeis University NSF MRSEC, DMR-1420382. Computational resources were provided by the NSF through XSEDE computing resources (Stampede) and the Brandeis HPCC which is partially supported by DMR-1420382. We gratefully acknowledge Robert Meyer, Robert Pelcovits, Zvonimir Dogic, and Prerna Sharma for helpful discussions; we also thank Prerna Sharma for providing her experimental data.

Appendix A: Non-dimensionalization of free energy

We begin with the free energy considered in the main text. With the one-constant approximation for the Frank free energy, and explicitly writing the constants r_0 and u_0 for the ψ^4 theory, this is given by

$$\beta F = \int d^2\mathbf{r} \quad \left\{ \begin{array}{r} \frac{K}{2}\left[(\nabla\cdot\hat{\mathbf{n}})^2 + (\hat{\mathbf{n}}\cdot\nabla\times\hat{\mathbf{n}} - q(\psi))^2 \right. \\ \left. + (\hat{\mathbf{n}}\times\nabla\times\hat{\mathbf{n}})^2\right] \\ + \frac{C}{2}\sin^2\theta + \frac{r_0\psi^2}{2} + \frac{u_0\psi^4}{4} + \frac{\lambda_\psi}{2}(\nabla\psi)^2 \end{array} \right\}$$

We then non-dimensionalize by rescaling all lengths with respect to the twist penetration depth $\lambda_t \equiv \sqrt{\frac{K}{C}}$, resulting in

$$\beta F = \int d^2\mathbf{r} \quad \left\{ \begin{array}{r} \frac{K}{2}\left[(\nabla\cdot\hat{\mathbf{n}})^2 + (\hat{\mathbf{n}}\cdot\nabla\times\hat{\mathbf{n}} - q(\psi))^2 \right. \\ \left. + (\hat{\mathbf{n}}\times\nabla\times\hat{\mathbf{n}})^2 + \sin^2\theta\right] \\ + \frac{\lambda_t^2 r_0\psi^2}{2} + \frac{\lambda_t^2 u_0\psi^4}{4} + \frac{\lambda_\psi}{2}(\nabla\psi)^2 \end{array} \right\}$$

We now substitute $q(\psi) = q_0 + a\psi$, collect the ψ^2 terms and (without loss of generality) set $\lambda_t r_0 = -1$ and $\lambda_t u_0 = 1$, resulting in

$$\beta F = \int d^2\mathbf{r} \quad \left\{ \begin{array}{r} \frac{K}{2}\left[(\nabla\cdot\hat{\mathbf{n}})^2 + (\hat{\mathbf{n}}\cdot\nabla\times\hat{\mathbf{n}} - q_0)^2 \right. \\ \left. + (\hat{\mathbf{n}}\times\nabla\times\hat{\mathbf{n}})^2 + \sin^2\theta\right] \\ -Ka\psi\left[\hat{\mathbf{n}}\cdot\nabla\times\hat{\mathbf{n}} - q_0\right] \\ -\frac{\psi^2 - Ka^2\psi^2}{2} + \frac{\psi^4}{4} + \frac{\lambda_\psi}{2}(\nabla\psi)^2 \end{array} \right\}$$

To keep the minima associated with our composition variable at ±1, we define $\psi' = \frac{\psi}{(1-Ka^2)^{1/2}}$. We then divide the entire free energy by $\left(1-Ka^2\right)^2$ and make the following transformations: $a' = a\left(1-Ka^2\right)^{1/2}$, $\lambda'_\psi = \frac{\lambda_\psi}{(1-Ka^2)}$ and $J = \frac{K}{(1-Ka^2)^2}$, $q'_0 = q_0(1-Ka^2)$. We then drop the $'$s and get the final free energy used in the rest of the discussion (Eq. 1 of the main text):

$$\beta F = \int d^2\mathbf{r} \quad \left\{ \begin{array}{r} \frac{J}{2}\left[(\nabla\cdot\hat{\mathbf{n}})^2 + (\hat{\mathbf{n}}\cdot\nabla\times\hat{\mathbf{n}} - q_0)^2 \right. \\ + (\hat{\mathbf{n}}\times\nabla\times\hat{\mathbf{n}})^2 + \sin^2\theta \\ \left. -2a\psi\,(\hat{\mathbf{n}}\cdot\nabla\times\hat{\mathbf{n}} - q_0)\right] \\ -\frac{\psi^2}{2} + \frac{\psi^4}{4} + \frac{\lambda_\psi}{2}(\nabla\psi)^2 \end{array} \right\}$$

Appendix B: Details of Linear Stability Analysis

In this section we provide details of the linear stability analysis leading to Eq. 4 in the main text. The dynamics of the director field, $\hat{\mathbf{n}}$ is described by:

$$\frac{\partial\hat{\mathbf{n}}}{\partial t} = \hat{\mathbf{n}}\times\hat{\mathbf{n}}\times\frac{\partial F}{\partial\hat{\mathbf{n}}}\ , \tag{B1}$$

where

$$\frac{\partial F}{\partial\hat{\mathbf{n}}} = -J\nabla^2\hat{\mathbf{n}} - 2Jq\nabla\times\hat{\mathbf{n}} + J\hat{\mathbf{n}}\times\nabla q + J(n_x\hat{x} + n_y\hat{y})\ , \tag{B2}$$

and $q = q_0 + a\psi$. The dynamics of the composition field ψ is described by:

$$\frac{\partial\psi}{\partial t} = \nabla^2\big(-Ja\hat{\mathbf{n}}\cdot(\nabla\times\hat{\mathbf{n}}) - \psi + \psi^3 - \lambda_\psi\nabla^2\psi\big) \tag{B3}$$

These equations admit homogeneous steady states of the form $\psi = \pm1$ and $\hat{\mathbf{n}} = \hat{\mathbf{z}}$. We linearize Eqs. B2 and B3 about a homogeneous solution and construct equations

for $\delta\psi = \psi - 1$ and $\delta n_x \hat{\mathbf{x}} + \delta n_y \hat{\mathbf{y}} = \hat{\mathbf{n}} - \hat{\mathbf{z}}$. The resulting linearized equations are:

$$\frac{\partial \delta n_x}{\partial t} = J\nabla^2 \delta n_x - J\delta n_x + Ja\partial_y \delta\psi \tag{B4}$$

$$\frac{\partial \delta n_y}{\partial t} = J\nabla^2 \delta n_y - J\delta n_y - Ja\partial_x \delta\psi \tag{B5}$$

$$\frac{\partial \delta\psi}{\partial t} = \nabla^2\big(-Ja(\partial_x \delta n_y - \partial_y \delta n_x) + 2\delta\psi - \lambda_\psi \nabla^2 \delta\psi\big) \tag{B6}$$

Introducing a fourier transform of the form $\widetilde{X}(\mathbf{k}, t) = \int d^2\mathbf{r} e^{i\mathbf{k}\cdot\mathbf{r}} X(\mathbf{r}, t)$ for the fields $\delta\hat{\mathbf{n}}$ and $\delta\psi$, and without loss of generality, choosing a coordinate system in the plane of the membrane such that the x axis lies along the spatial gradient direction $\mathbf{k}$, we obtain:

$$\partial_t \begin{pmatrix} \delta\widetilde{\psi} \\ \delta\widetilde{n}_x \\ \delta\widetilde{n}_y \end{pmatrix} = \begin{pmatrix} -2k^2 - \lambda_\psi k^4 & 0 & -ik^3 Ja \\ 0 & -J - Jk^2 & 0 \\ ikJa & 0 & -J - k^2 J \end{pmatrix} \begin{pmatrix} \delta\widetilde{\psi} \\ \delta\widetilde{n}_x \\ \delta\widetilde{n}_y \end{pmatrix} \tag{B7}$$

We observe from Eq. B7 that the δn_x fluctuations decouple from the other fluctuations and the linearized problem of interest reduces to:

$$\begin{bmatrix} \dfrac{\partial \delta\widetilde{\psi}}{\partial t} \\ \dfrac{\partial \delta\widetilde{n}_y}{\partial t} \end{bmatrix} = \begin{bmatrix} -2k^2 - \lambda_\psi k^4 & iJak^3 \\ -iJak & -Jk^2 - J \end{bmatrix} \begin{bmatrix} \delta\widetilde{\psi} \\ \delta\widetilde{n}_y \end{bmatrix} \tag{B8}$$

The eigenvalues $\omega(k)$ of the matrix determine if and for what values of the parameters the homogeneous state becomes unstable to one of these k-modes. The mode with the largest positive value of $\omega(k)$ defines the leading instability.

The eigenvalues of the matrix satisfy:

$$(2k^2 + \lambda_\psi k^4 + \omega(k))(Jk^2 + J + \omega(k)) - J^2 a^2 k^4 = 0 \tag{B9}$$

We show plots of the numerical solutions for the dispersion relation $\omega(k)$ for a few values of J and a in the main text. It is clear from this equation that the $k = 0$ mode is marginally stable for all parameters and that the leading instability occurs at a *finite* value of k and is determined by values of (J, a, λ) that simultaneously satisfy (i) $\frac{\partial\omega(k)}{\partial k} = 0$ and (ii) $\omega(k) = 0$. The linear stability analysis thus clearly indicates that there is a discontinuous change in k and, therefore, implies that the droplet radius should change discontinuously at the transition from bulk phase separation (all nonzero k modes stable) to microphase separation.

We can calculate the wavevector $k_{\rm f}$ characterizing the growing mode at the onset of the instability from Eq. B9. Condition (ii) implies:

$$\lambda_\psi k_{\rm f}^4 - (Ja^2 - 2 - \lambda_\psi)k_{\rm f}^2 + 2 = 0$$

The roots of this equation at nonzero k are:

$$k_{\rm f}^2 = \frac{(Ja^2 - 2 - \lambda_\psi)}{2\lambda_\psi}\Big(1 \pm \frac{\sqrt{(Ja^2 - 2 - \lambda_\psi)^2 - 8\lambda_\psi}}{(Ja^2 - 2 - \lambda_\psi)}\Big) \tag{B10}$$

At the onset of the instability, these two roots have to be degenerate (the condition for $\omega(k_{\rm f})$ having a maximum), which implies that:

$$(Ja^2 - 2 - \lambda_\psi)^2 = 8\lambda_\psi \ .$$

Therefore,

$$k_{\rm f} = (\frac{2}{\lambda_\psi})^{1/4}$$

The fastest growing wavelength, and therefore the optimum droplet size in the microphase separated regime thus depends only on λ_ψ, and the boundary marking the onset of the instability is given by $(Ja^2 - 2 - \lambda_\psi) = \sqrt{8\lambda_\psi}$.

Appendix C: Quasistatic calculation

To better understand the origin of the microphase separation with a discontinuous change in the domain size, we calculate the free energy density, $f(R)$ of a circular droplet of radius R with $\psi = 1$ in a background of $\psi = -1$. A diffuse interface between the drop and the background is initialized using the radially symmetric function $\psi(r) := \tanh\Big(\frac{x}{\sqrt{2}\lambda_\psi}\Big)$. This represents the solution to $\frac{\delta F_\psi[\psi]}{\delta\psi} = 0$ (see [30]). A drop of radius R is placed inside a larger system of radius $R_{\rm sys}$, chosen to be 5 twist penetration lengths ($\lambda_{\rm t}$) larger than R. The director profile is then obtained by numerically equilibrating the GL equations for the director field with the prescribed static order parameter field ψ. The numerical solutions to the GL equations show that : i) on average, the domains are circularly symmetric, ii) the tilt of the director is tangential to the edge of the disk, and iii) droplets of the same radius R at two different values of the parameter set exhibit the same functional form of the tilt profile. Thus, the numerically obtained profiles for the twist in $\hat{\mathbf{n}}$ are only a function of the radius R. Choosing a cylindrical coordinate system, the director can be represented as $\vec{n} = sin(\theta)\hat{\phi} + cos(\theta)\hat{z}$. For a circularly symmetric tilt profile, the different contributions to the free energy can be written in these coordinates as

$$\begin{aligned} F_{\rm LC} &= \int_0^{R_{sys}} \Big[\frac{1}{2}J\Big(\frac{d\theta}{dr} + \frac{sin(2\theta)}{2r} - q_0\Big)^2 \\ &\qquad + \frac{1}{2}J\frac{sin^4(\theta)}{r^2}\Big] 2\pi r dr, \\ F_{\rm Cross} &= \int_0^{R_{sys}} \Big[\frac{1}{2}J\Big(\frac{d\theta}{dr} + \frac{sin(2\theta)}{2r} - a\psi\Big)^2\Big] 2\pi r dr, \\ F_\psi &= \int_0^{R_{sys}} \Big[-\frac{\psi^2}{2} + \frac{\psi^4}{4} + \frac{\lambda_\psi}{2}\left(\frac{d\psi}{dr}\right)^2\Big] 2\pi r dr \end{aligned} \tag{C1}$$

These expressions are evaluated using the numerically obtained profiles $\theta(r)$ and $\psi(r)$ for a droplet of radius R and are reported and discussed in the main text.

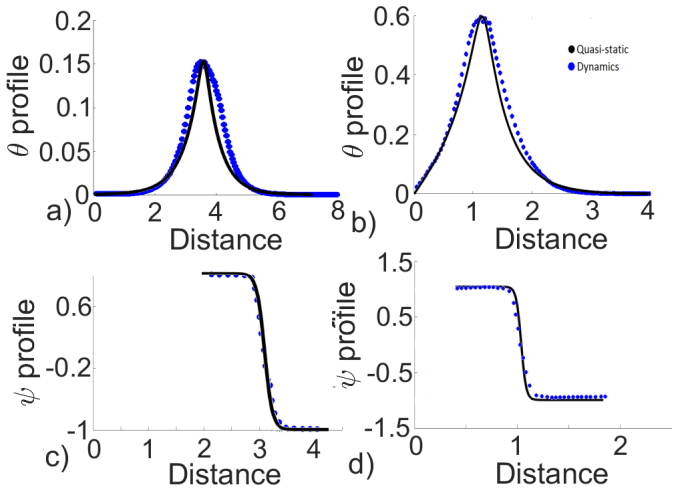

FIG. 5. (color online) Comparison of twist and ψ profiles predicted by the quasistatic calculation (black line) with results from the numerical integration of the full model dynamics (blue dots). The profiles from the dynamics are ensemble-averaged over droplets of the same size in equilibrium configurations. a) Twist profiles for droplets with radius greater than twist penetration depth λ_t. b) Twist profiles for droplets with radius smaller than λ_t, exhibiting a cutoff of the exponential decay inside the droplet. c) ψ profile for droplets with radius larger than λ_t. d) ψ profile for droplets with radius smaller than λ_t.

Note that we consider a single droplet in an infinite background in the quasistatic calculation, whereas the full set of equations models systems with multiple droplets. Thus, we are neglecting the effect of interactions between droplets in the quasistatic model. As noted in the main text, this choice is made to focus the quasistatic calculation on the physical mechanisms that affect droplet size. Existing experimental and theoretical results indicate that inter-droplet interactions only become significant at smaller inter-droplet spacings than arise in our dynamical simulations [12, 14]. Moreover, a comparison of the quasistatic calculation with the ensemble averaged profiles (ψ and θ) of equilibrium droplets of the same size from the dynamical simulations (which do include inter-droplet interactions) shows semi-quantitative agreement (Fig. 5). In particular it is worth noting that the twist decays rapidly with exponential decay into the background even in the presence of neighboring drops in the dynamical simulations. Further, Fig. (6) shows that order parameter profile does not depend strongly on the parameters J and a. This result can be understood by noting that the order parameter profile in the dynamical simulations is controlled primarily by minimization of F_ψ; the cross terms which couple ψ to twist only weakly affect the spatial variation of ψ.

As noted in the main text, this quasistatic calculation shows that the source of the super-extensive growth in the free energy densities $f_{\rm LC}$ and $f_{\rm Cross}$, and the eventual asymptote to extensive growth, can both be understood from the dependence of twist profiles on R (Fig. (6),(5)). For large domains, twist decays exponentially from the domain edge, while for small domains , the twist penetrates into the center of the domain and thus contributes to the bulk free energy.

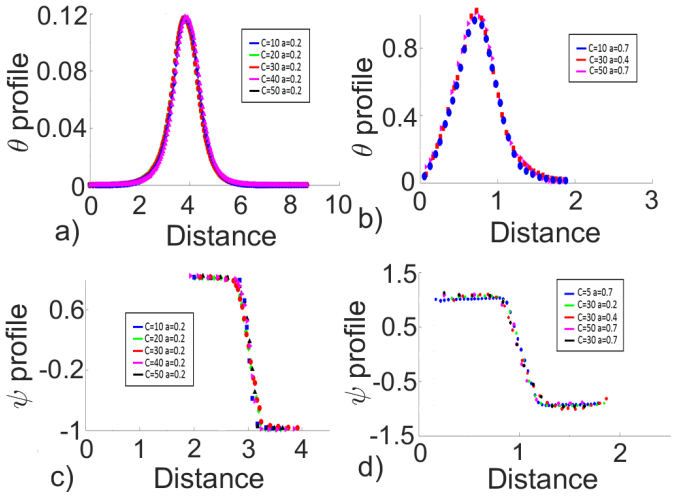

FIG. 6. (color online) Dependence of twist and ψ profiles on J and a obtained from dynamical simulations by ensemble-averaging over equilibrium droplets of same size. a) Twist profiles for droplets with radius greater than twist penetration depth λ_t for indicated values of J and a. b) Twist profiles for droplets with radius smaller than λ_t, exhibiting a cutoff of the exponential decay inside the droplet. c) ψ profile for droplets with radius larger than λ_t. d) ψ profile for droplets with radius smaller than λ_t.

Note that near the edge of a domain, the twist becomes sufficiently large that the present theory may become inaccurate. Additional terms could be added to the free energy following the approach of Kaplan et al. [24]. However, this cannot change the basic mechanism identified here since this region is confined to the very edge of a domain, whereas the stabilization of finite -sized domains arises due to penetration of some twist all the way into a domain interior.

Appendix D: Effect of varying λ_ψ and q_0

We performed additional sets of numerical integration and additional linear stability analyses to determine the effect of the parameters λ_ψ and q_0 on phase behavior and droplet sizes. As shown in the main text, the onset of the instability depends on λ_ψ according to $(Ja^2-2-\lambda_\psi)^2 =$

$8\lambda_\psi$. The phase boundary from numerics is shown for two distinct values of λ_ψ in Fig. 7b.

As shown in Fig. 7a, the width of the droplet interface is roughly proportional to λ_ψ, while it is independent of chirality and bending modulus (Fig. 6).

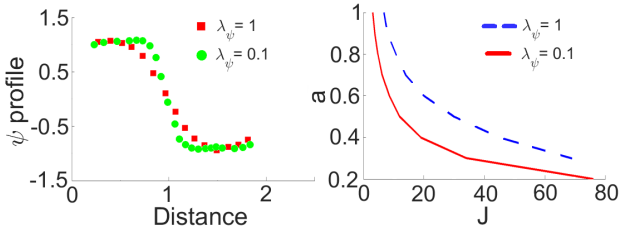

FIG. 7. (color online) a) Change in ψ profile as a function of λ_ψ for droplets of the same size normalized to 1 for $J = 40$ and $a = 0.6$, calculated by numerical simulations. b) Location of the boundary between micro and bulk phase-separation calculated by numerical simulations for $\lambda_\psi = 0.1$ (red/solid) and $\lambda_\psi = 1$ (blue/dashed)

We also performed numerical integration of the dynamical equations for different values of the chirality offset parameter q_0. Although this parameter does not affect the instability to linear order, the results from the dynamical simulation show that it shifts the instability to larger values of a, as shown in Fig. 8. =

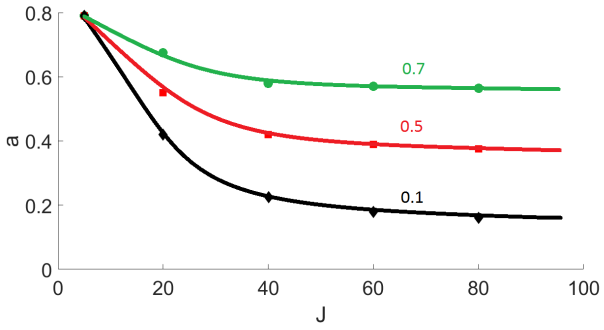

FIG. 8. (color online) Location of the boundary between micro and bulk phase-separation for $q_0 = 0.1$ (lower line), $q_0 = 0.5$ (middle line) and $q_0 = 0.7$ (upper line) for $\lambda_\psi = 0.1$ calculated from the numerical simulations. The line is a polynomial interpolation to serve as a guide to the eye.

Appendix E: Numerical Method

In order to numerically time evolve the coupled equations (2-3) in the main text, we consider a periodic domain $\Omega := [0, L_x] \times [0, L_y]$. The domain is discretized with a uniform mesh of spacing h such that $L_x = m \cdot h$ and $L_y = n \cdot h$. Thus the points on the uniform mesh are given by $\mathbf{x}_{ij} = (x_i, y_j)^T$ where $x_i = 0 + i \cdot h$, $y_j = 0 + j \cdot h$ and $1 \le i \le m, 1 \le j \le n$ are integers. For simplicity we denote scalar valued functions on this mesh as $f_{ij} = f(x_i, y_j)$. Now the discrete laplacian of the scalar field f at (x_i, y_j) is defined as :

$$\Delta_h f_{ij} = \frac{1}{h^2}\left(f_{i+1,j} + f_{i-1,j} + f_{i,j+1} + f_{i,j-1} - 4f_{ij}\right) \tag{E1}$$

and the discrete gradient is given by

$$\nabla_h f_{ij} := \left(\frac{1}{2h}\left(f_{i+1,j} - f_{i-1,j}\right), \frac{1}{2h}\left(f_{i,j+1} - f_{i,j-1}\right)\right)^T. \tag{E2}$$

These represent the central difference approximations for the derivatives, and other gradient operators including the curl are computed in a self consistent manner. We refer the interested reader to [31] (see Appendix E) for details of the discrete spaces, operators and implementation of boundary conditions. Finally we use a uniform discretization of time $t_k := 0 + k \cdot s$, where $s > 0$ is the time step and k is a positive integer. We now represent the fully discrete scalar function at (x_i, y_j) at time t_k by $f(t_k, x_i, y_j) := f_{ij}^k$ to simplify the notation. Given $\hat{\mathbf{n}}_{ij}^k$ and ψ_{ij}^k we use a classic forward Euler approximation for time stepping vector field $\hat{\mathbf{n}}$ to obtain $\hat{\mathbf{n}}_{ij}^{k+1}$. The phase field ψ (Cahn Hilliard type equation) can in principle be time evolved using a forward Euler method. This however leads to severe time step restrictions i.e., $s \sim O(h^4)$ for numerical stability (see [32]). In order to improve the efficiency we use a semi-implicit convex splitting approach proposed by D. Eyre in [32] (also see [31], Section 3 for generalizations). This scheme is unconditionally stable and presents no time step restrictions for the Cahn Hilliard equations.

Thus given ψ_{ij}^k and $\hat{\mathbf{n}}_{ij}^{k+1}$, the latter obtained from a forward Euler method, we use the following scheme to obtain ψ_{ij}^{k+1} :

$$\begin{aligned} \psi_{ij}^{k+1} - \psi_{ij}^k &= s\Delta_h \mu_{ij}^{k+1}, \\ \mu_{ij}^{k+1} &= \left(-\psi_{ij}^k + (\psi_{ij}^{k+1})^3 - \lambda_\psi \Delta_h \psi_{ij}^{k+1}\right. \\ &\quad \left. - Ja\left(\hat{\mathbf{n}}_{ij}^{k+1} \cdot \nabla_h \times \hat{\mathbf{n}}_{ij}^{k+1}\right)\right). \end{aligned} \tag{E3}$$

The above equations are solved using a Full Approximation Storage (FAS) non-linear multigrid algorithm with a Gauss Seidel smoothing scheme. We used a grid of 512×512 with a grid size of 0.1 in terms of the twist penetration length and a time step of the order of the distance.

[1] S. Safran, *Statistical thermodynamics of surfaces, interfaces, and membranes* (Westview press, 2003).
[2] A. A. Hyman and K. Simons, Science **337**, 1047 (2012).
[3] D. Lingwood and K. Simons, Science **327**, 46 (2010).
[4] R. M. Weis and H. M. McConnell, Nature **310**, 47 (1983).
[5] C. Dietrich, L. Bagatolli, Z. Volovyk, N. Thompson, M. Levi, K. Jacobson, and E. Gratton, Biophysical journal **80**, 1417 (2001).
[6] K. Simons and M. J. Gerl, Nature reviews Molecular cell biology **11**, 688 (2010).
[7] S. L. Veatch and S. L. Keller, Biophysical journal **85**, 3074 (2003).
[8] T. Gibaud, E. Barry, M. J. Zakhary, M. Henglin, A. Ward, Y. Yang, C. Berciu, R. Oldenbourg, M. F. Hagan, D. Nicastro, R. B. Meyer, and Z. Dogic, Nature **481**, 348 (2012).
[9] M. J. Zakhary, P. Sharma, A. Ward, S. Yardimici, and Z. Dogic, Soft Matter **9**, 8306 (2013).
[10] M. J. Zakhary, T. Gibaud, C. Nadir Kaplan, E. Barry, R. Oldenbourg, R. B. Meyer, and Z. Dogic, Nature Communications **5**, 3063 EP (2014).
[11] E. Barry, D. Beller, and Z. Dogic, Soft Matter **5**, 2563 (2009).
[12] P. Sharma, A. Ward, T. Gibaud, M. F. Hagan, and Z. Dogic, Nature **513**, 77 (2014).
[13] E. Barry and Z. Dogic, Proceedings of the National Academy of Sciences **107**, 10348 (2010).
[14] S. Xie, M. F. Hagan, and R. A. Pelcovits, Phys. Rev. E **93**, 032706 (2016).
[15] J. V. Selinger, Z.-G. Wang, R. F. Bruinsma, and C. M. Knobler, Physical review letters **70**, 1139 (1993).
[16] F. Elias, C. Flament, J.-C. Bacri, and S. Neveu, Journal de Physique I **7**, 711 (1997).
[17] F. S. Bates and G. H. Fredrickson, Physics today **52**, 32 (2008).
[18] M. Seul and D. Andelman, Science **267**, 476 (1995).
[19] T. Janssen, G. Chapuis, and M. De Boissieu, *Aperiodic crystals: from modulated phases to quasicrystals* (Oxford University Press Oxford, 2007).
[20] G. M. Grason and R. F. Bruinsma, Phys. Rev. Lett. **99**, 098101 (2007).
[21] M. M. A. E. Claessens, C. Semmrich, L. Ramos, and A. R. Bausch, Proceedings of the National Academy of Sciences **105**, 8819 (2008), http://www.pnas.org/content/105/26/8819.full.pdf.
[22] P.-G. De Gennes and J. Prost, *The physics of liquid crystals* (Clarendon press Oxford, 1993).
[23] R. A. Pelcovits and R. B. Meyer, Liquid Crystals **36**, 1157 (2009).
[24] C. N. Kaplan, H. Tu, R. A. Pelcovits, and R. B. Meyer, Physical Review E **82**, 021701 (2010).
[25] C. N. Kaplan and R. B. Meyer, Soft matter **10**, 4700 (2014).
[26] L. Kang, T. Gibaud, Z. Dogic, and T. C. Lubensky, Soft Matter **12**, 386 (2016).
[27] L. Kang and T. C. Lubensky, Proceedings of the National Academy of Sciences **114**, E19 (2017).
[28] P. C. Hohenberg and B. I. Halperin, Reviews of Modern Physics **49**, 435 (1977).
[29] We note that the homogeneous state is always unstable by construction since we focus on parameters that lead either to microphase or macrophase separation. The objective of the linear stability analysis is to identify the fastest growing length scale of phase separation.
[30] N. Provatas and K. Elder, *Phase-field methods in materials science and engineering* (John Wiley & Sons, 2011).
[31] A. Baskaran, Z. Guan, and J. Lowengrub, Computer Methods in Applied Mechanics and Engineering **299**, 22 (2016).
[32] D. J. Eyre, MRS Proceedings **529** (2011), 10.1557/PROC-529-39.